A Bidirectional Series Z-Source Circuit Breaker

Daniel Joseph Ryan, *Student Member, IEEE*, Hugh Duffy Torresan, *Member, IEEE*, and Behrooz Bahrani, *Member, IEEE*

***Abstract*—A Z-source series circuit breaker topology, which allows bidirectional power flow and has the ability to autonomously disconnect dc faults, is introduced. This topology allows current flow in the forward and reverse directions through the use of a diode bridge. The diode bridge allows response to faults on either the source or load side with only a single controlled switch. No additional passive components are required when compared with the unidirectional series Z-source circuit breaker topology. Analysis is performed to find the fault conditions that cause the bidirectional circuit breaker to trip when operating in a single-load power system. Then, using the simulation platform MATLAB/Simulink, operation of the bidirectional circuit breaker is evaluated for both source- and load-side faults. To experimentally validate the findings, an experimental prototype has been implemented. This prototype is used to confirm the circuit breaker's function in both the forward and reverse directions in addition to its response to source-side faults.**

***Index Terms*—Bidirectional circuit breaker, dc systems, power electronic circuit breaker (PECB), protection systems, Z-source circuit breaker (ZCB).**

I. Introduction

RECENTLY, there has been a trend toward using direct current (dc) in power systems. Applications being investigated are electric ships [1], high-voltage dc networks [2], microgrids [3], [4], data centers [5], battery energy storage [6], and wind farms [7]. However, viability of applications that use medium-voltage dc (MVDC) is limited by current dc circuit breaker (CB) technology.

Protection of low-voltage dc systems is commonly achieved using arc-based circuit breakers (ACBs). However, dc systems lack a natural zero-current crossing, which increases the difficulty of extinguishing the arc generated when the ACB opens [8]. Thus, as voltage and fault current increase, the size and cost of such ACBs become prohibitive. Thus, MVDC systems require a novel solution.

Power electronic circuit breakers (PECBs) are an alternative to ACBs, which use semiconductors rather than mechanical switches. The series and parallel connection of semiconductor devices provides scalability. This allows PECBs to operate in MVDC systems, which operate at higher voltage and fault current levels than are feasible for ACBs [9]. Additionally, PECBs can limit fault currents, due to their high operating speed [10]–[12].

Although PECBs provide these advantages, they require additional sensing and control circuitry, have power loss in the semiconductor junctions, lack galvanic isolation, and have low fault current capability. Thus, there has been significant research effort to address these issues.

In order to increase the efficiency of PECBs, use of custom silicon [13] or widebandgap semiconductors [14]–[17] has been investigated. However, currently, the availability of these semiconductor devices is limited, particularly at high voltage and current levels. Another alternative can be hybrid CBs, which combine an ACB and PECB in parallel [18]–[23]. Hybrid CBs provide efficiency similar to ACBs. However, they are costly and have increased response time compared with PECBs. This makes managing fault currents in the semiconductor switch difficult.

Additionally, the fault detection and control system required for PECBs increases response time, increases cost, and adds a point of failure. To address this, Z-source circuit breakers (ZCBs), a type of PECB that autonomously respond to faults, are proposed [24], [25]. Autonomous operation lowers response time, reduces sensing and processing electronics, and limits fault current. Additionally, passive components used in ZCBs limit the peak current in the semiconductor switch, so that it is not required to withstand high fault currents. Thus, ZCBs address two of the four issues mentioned above. Furthermore, in order to lower loss in a ZCB, it is possible to integrate modern semiconductor devices into the ZCB [13]. Moreover, a simple no-load switch can be used to provide galvanic isolation for safety reasons, opening once the fault current is broken.

In order to improve upon the first proposed ZCBs, the series ZCB topology, shown in Fig. 1, is proposed in [26] and [27]. When compared with other ZCBs, it maintains a common neutral between the input and output. Additionally, its transfer function is that of a second-order low-pass filter, which is suitable for input filtering of power electronic converters. This allows the CB to serve two purposes: 1) fault protection and 2) filtering. Integrating the CB into the input filter of power electronic converters reduces the number of components and cost of a dc power system. Furthermore, the peak source current during fault interruption is reduced compared to some other ZCB topologies.

In [28], a modified series ZCB is proposed for discrimination between load steps and faults. In [29], a series ZCB with

Manuscript received May 22, 2017; revised August 18, 2017; accepted October 16, 2017. Date of publication October 22, 2017; date of current version June 22, 2018. This work was supported by the Defence Science and Technology Group, Australia. Recommended for publication by Associate Editor D. Dujic. *(Corresponding author: Daniel Joseph Ryan.)*

D. J. Ryan and B. Bahrani are with the Department of Electrical and Computer Systems Engineering, Monash University, Melbourne, VIC 3800, Australia (e-mail: daniel.ryan@monash.edu; behrooz.bahrani@monash.edu).

H. D. Torresan is with the Defence Science and Technology Group, Melbourne, VIC 3207, Australia (e-mail: hugh.torresan@dsto.defence.gov.au).

Color versions of one or more of the figures in this paper are available online at http://ieeexplore.ieee.org.

Digital Object Identifier 10.1109/TPEL.2017.2764903

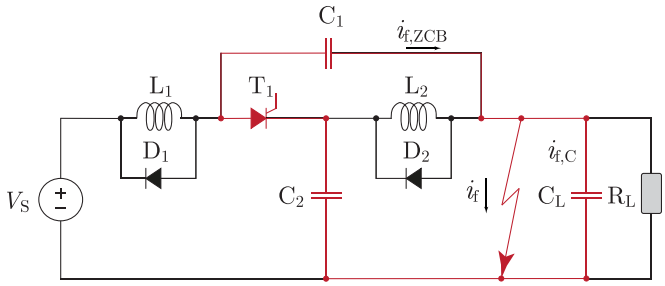

Fig. 1. Fault current path of unidirectional series ZCB [27].

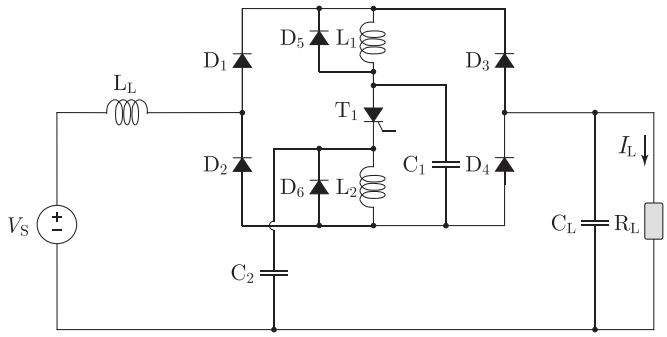

Fig. 2. Steady-state current flow of the proposed topology.

mutually coupled inductors is proposed for reduced volume and weight. However, none of the proposed series ZCBs allow bidirectional power flow. The capability of operating with bidirectional power flow is an increasingly common requirement for modern power systems. Driving this increase is the expanding use of energy storage systems, redundant network structures such as the ring bus, and grid-connected microgrids, which may either absorb or supply power from their point of common coupling. System protection must take this requirement into account.

This paper introduces a bidirectional series ZCB, which is scalable for MVDC systems. The proposed ZCB retains the advantages of the series ZCB including common neutral, reduced peak source current, and a low-pass filter frequency response characteristic. In this paper, the performance of the proposed ZCB in a simple power system is theoretically analyzed, and several expressions for various operating scenarios of the ZCB are developed. The expressions derived are validated with simulated results. Additionally, experimental results of the bidirectional series ZCB are presented, which validate its operation in both the forward and reverse directions and its response to source side faults.

This paper is structured as follows. Section II describes the introduced bidirectional series ZCB topology and its operational principles and provides an analysis of various fault conditions. Section III provides a comparison of the proposed bidirectional series ZCB topology with competing bidirectional Z-source topologies. In Section IV, the performance of the proposed ZCB is validated through simulation and experimental results. Section V concludes this paper.

II. Bidirectional Series ZCB Topology

The proposed bidirectional series ZCB is shown in Fig. 2. The full-bridge arrangement of diodes allows load current to flow in either direction, while retaining the same conduction path through the Z-source inductors and thyristor. Thus, the CB limits and interrupts fault current regardless of the direction of power flow. Additionally, the CB responds to faults on either set terminals.

A description of the CB's on-state operation is given in Section II-A. Section II-B gives a description of the CB's response to output faults. This is followed by a derivation of the CB's minimum output fault conductance in Section II-C and minimum detectable output fault ramp-rate (Frr) in Section II-D. Section II-E gives a description of the CB's response to input faults. This is followed by a derivation of the CB's minimum input fault conductance in Section II-F and minimum detectable input Frr in Section II-G. Finally, in Section II-H, the maximum voltage and current stresses for the components of the CB are tabulated.

The minimum detectable Frr and fault conductance are required in selection of the CB's passive components to find the fringe cases for fault detection. They also define the maximum allowable load current slew rate and load step change. In the analysis performed, it is assumed that $C_1 = C_2 = C_{ZCB}$ and $L_1 = L_2 = L$. The investigation is undertaken with a bidirectional series ZCB in a simple power system, which is shown in Fig. 2. In this system, the ZCB is protecting an *RC* load, which is being supplied by an ideal dc voltage source and a line with inductance L_L. The load capacitance C_L represents the typically large input capacitance of a voltage-fed power electronic converter. In order for the CB to switch from the OFF state to the ON state, T_1 is gated ON. The gating signal can be released once the CB reaches a steady state.

A. On-State Operation

In the ON state (see Fig. 2), the line inductances L_L, L_1, and L_2 pass the steady-state load current I_L, and the voltage drop across the inductances is zero. D_1 and D_4 are conducting, while D_2 and D_3 are in the reverse-blocking state. Assuming ideal components, the load voltage is V_S, C_2 is charged to V_S, and C_1 is discharged. If the source and load connections are swapped, the CB behaves in the same manner. However, D_2 and D_3 are in the forward-conducting state, while D_1 and D_4 are in the reverse-blocking state.

In an application such as protection of energy storage, where the power flow may gradually change from one direction to another, T_1 may switch OFF when the current flow direction reverses. This is because as the power flow direction reverses, the load current must drop momentarily to zero. The thyristor has a specified turn-off time t_q and holding current i_H. If the thyristors current is allowed to fall below i_H for a period longer than t_q, it switches to the blocking state. To avoid this, the CB's control system must provide a gating signal to T_1 when the power flow direction changes.

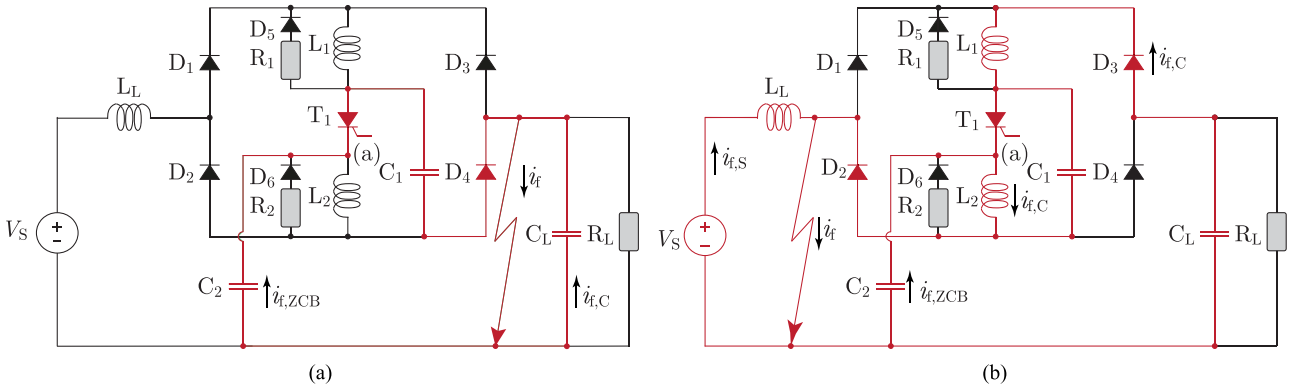

Fig. 3. Fault current flow of the proposed topology for (a) a fault on the input and (b) a fault on the output.

B. Response to Output Faults

When a fault is applied to the CB's output, while it is operating in the ON state, the fault current flows through the red path shown in Fig. 3(a). The fault current is divided into $i_{f,ZCB}$ and $i_{f,C}$; $i_{f,ZCB}$ flows through the Z-source capacitors, and $i_{f,C}$ flows through the load capacitance. When the fault first occurs, the Z-source inductors resist a change in current; thus, their currents remain at their prefault level I_L. Inspecting the node (a) current, as shown in Fig. 3(a), when $i_{f,ZCB}$ rises to I_L, i_T is zero causing T_1 to commutate OFF. Once T_1 turns OFF, two series LC circuits are formed: 1) through L_1, C_1, and the fault, and 2) through L_2, C_2, and the fault. With typical component values, both circuits have underdamped resonant responses, which are decoupled when the fault impedance is zero. The initial conditions for resonance are determined by the steady-state operating point of the circuit.

When these circuits begin to resonate, v_{C_2} falls, and v_{C_1} rises. When v_{C_1} rises above V_S, the inductor voltages fall below zero and are clamped by diodes D_5 and D_6. This restricts the thyristor voltage from rising above the source voltage, which lowers the forward-blocking voltage requirement of T_1 to V_S. The inductor current is clamped at the current peak of the LC circuit; thus, the stored energy of the circuits is dissipated in the clamping diodes (D_5 and D_6). In practice, a resistor could be added in series with the clamping diode, as shown in Fig. 3(a), in order to dissipate the stored energy more quickly. However, the resistor's voltage drop increases the blocking requirement of the thyristor.

During the resonance, the output diode (D_2 or D_4) current is the sum of the current in the two series LC circuits. The input diode (D_1 or D_3) current is only that of one series LC circuit; thus, it is half of the output diode current. Note that the reverse recovery time of the diodes does not affect the CB's operation; thus, low-loss standard recovery diodes are suitable. Additionally, the forward voltage drop of a diode is generally lower than that of an equivalently rated thyristor.

C. Minimum Detectable Fault Conductance—Output

The CB's response to a fault depends on the characteristics of the fault and the power system within which it is operating. For the CB to operate autonomously, these characteristics must be such that the current through T_1 falls to zero subsequent to a fault. The requirements for autonomous operation, in the case where a fault with conductance G_f is applied at $t = 0$ μs at the CB's output, are investigated for the power system shown in Fig. 3(a). Thus, the minimum fault conductance ($G_{f,min,out}$), which causes the CB to trip, is derived. Assuming a fault at the CB output, the fault current can be written as

$$i_f(t) = v_f(t)G_f. \tag{1}$$

Through analysis of the fault node, where load current and inductor current are assumed to be equal, it is found that

$$i_f(t) = i_{f,ZCB}(t) + i_{f,C}(t). \tag{2}$$

Assuming $C_1 = C_2 = C_{ZCB}$ and substituting for i_F from (1) in (2) result in

$$G_f v_f(t) = -\frac{C_{ZCB}}{2}\frac{dv_f(t)}{dt} - C_L\frac{dv_f(t)}{dt}. \tag{3}$$

Assuming a lossless CB, C_L is charged to V_S during steady-state operation. Thus, the initial condition is

$$v_f(0) = V_S. \tag{4}$$

Through solving (3) with the initial condition (4), we have

$$v_f(t) = V_S e^{-\frac{2G_f}{C_{ZCB}+2C_L}t}. \tag{5}$$

Thus, using

$$i_C(t) = C\frac{dv_C(t)}{dt} = \frac{C_{ZCB}}{2}\frac{dv_f(t)}{dt} \tag{6}$$

it is found that

$$i_{f,ZCB}(t) = V_S\frac{C_{ZCB}G_f}{C_{ZCB}+2C_L}e^{-\frac{2G_f}{C_{ZCB}+2C_L}t}. \tag{7}$$

From (7), $i_{f,ZCB}(t)$ is a decaying exponential. Thus, it is maximum for $t = 0$ μs. For i_{T_1} to fall to zero, the ZCB fault current must overcome the steady-state load current. Therefore, to trip, $i_{f,ZCB}$ must be larger than I_L. The steady-state load current (I_L) is

$$I_L = \frac{V_S}{R_L}. \tag{8}$$

Thus, $G_{f,min,out}$ is found where $i_1(0) = I_L$ and is described as follows:

$$G_{f,min,out} = \left(1 + \frac{2C_L}{C_{ZCB}}\right) \cdot \left(\frac{1}{R_L}\right). \tag{9}$$

$G_{f,min,out}$ decreases as C_{ZCB} increases relative to C_L. This is because a larger portion of the initial fault current flows through the Z-source capacitors. $G_{f,min,out}$ also decreases as R_L increases. This is due to a decrease in steady-state load current, which reduces the magnitude of $i_{f,ZCB}$ required to commutate T_1 OFF. When C_L is zero, $G_{f,min,out}$ is equal to the load conductance G_L. Assuming that the load capacitance is known, which is likely for power electronic loads, and taking the maximum steady-state load (worst case), (9) allows the selection of C_1 and C_2 to meet a required minimum $G_{f,min,out}$.

D. Minimum Detectable Frr – Output

In this section, the minimum detectable output Frr, $K_{rr,min,out}$, is derived. The fault conductance G_f is dependent on time t with a linear gradient of K_{rr}; thus

$$i_f(t) = G_f(t)v_f(t) = K_{rr}t \cdot v_f(t). \tag{10}$$

A linearly increasing conductance approximates the behavior of an inductor as follows:

$$i_L(t) = \frac{1}{L}\int_0^t V_L dt + i_L(0). \tag{11}$$

With a constant applied voltage V_L and zero initial current $i_L = 0$ A, the inductor characteristic is reduced to

$$\Delta i_L(t) = V_L \frac{1}{L}\Delta t. \tag{12}$$

Substituting for G_f from (10) into (3) results in

$$K_{rr}\, t\, v_f(t) = -\frac{C_{ZCB}}{2}\frac{dv_f}{dt} - C_L\frac{dv_f}{dt}. \tag{13}$$

Solving (13) for the initial conditions defined in (4) gives

$$v_f(t) = V_S e^{-\frac{K_{rr}}{C_{ZCB} + 2C_L}t^2}. \tag{14}$$

Substituting for $v_f(t)$ from (14) into (6) results in

$$i_{f,ZCB}(t) = V_S \frac{C_{ZCB}\,K_{rr}}{C_{ZCB} + 2C_L} t e^{-\frac{K_{rr}}{C_{ZCB} + 2C_L}t^2}. \tag{15}$$

Thus, the instant at which $i_{f,ZCB}(t)$ has its maximum is found as follows:

$$t_{max} = \sqrt{\frac{2C_L + C_{ZCB}}{2K_{rr}}}. \tag{16}$$

The minimum Frr $K_{rr,min}$ is, therefore, found, where $i_{f,ZCB}(t_{i_1,max})$ is equal to the steady-state load current I_L. Thus

$$K_{rr,min,out} = 2e\frac{C_{ZCB} + 2C_L}{R_L^2\, C_{ZCB}^2}. \tag{17}$$

In [27], an expression for the minimum detectable Frr of a unidirectional series Z-source CB feeding an RC load is derived. This is equivalent to the expression (17) of the bidirectional series Z-source CB. Similarly to $G_{f,min,out}$, $K_{rr,min,out}$ is dependent on R_L. In both cases, the minimum value of R_L represents the worst-case scenario, where the CB is least likely to trip. Additionally, nuisance tripping may be caused by high slew rates of load current. Thus, a restriction of

$$\frac{di_{load}}{dt} < V_{out}K_{rr,min,out} \tag{18}$$

is placed on the current slew rate of the load. This stops unwanted tripping of the CB. Equation (18) is equivalent to stating that a change in load conductance must have a ramp rate less than $K_{rr,min,out}$.

E. Response to Input Faults

The proposed CB is also able to operate autonomously for faults on its input, regardless of initial current flow direction. This allows rapid and autonomous isolation of faulted lines from a dc power system. If the CB is in the ON state and a fault is applied across its input, some of the initial fault current is supplied by the Z-source capacitors. The response of other components is dependent on the load capacitance as described in the following.

1) RC Load: In the case where a short-circuit fault occurs and there is a load capacitance, fault current flows, as shown in Fig. 3(b). The initial fault current is the sum of $i_{f,ZCB}$, $i_{f,C}$, and $i_{f,S}$. In this case, the collapsing input voltage causes D_1 and D_4 to turn OFF and D_3 and D_2 to turn ON. The initial fault current supplied by the dc source ($i_{f,S}$) is limited to I_L by the line inductance. Similarly, the initial fault current ($i_{f,C}$) supplied by C_L is limited to I_L by the Z-source inductors. Additionally, the Z-source capacitance supplies the fault current $i_{f,ZCB}$. Inspecting the cathode current of T_1, when i_1 is equal to I_L (the current through L_2), T_1 current falls to zero commutating it OFF. When T_1 turns OFF, two series LC resonant circuits are formed: 1) through C_2, L_2, and the fault, and 2) through C_1, C_L, L_1, and the fault. These circuits are decoupled when the fault impedance is zero. The initial conditions for resonance are determined by the steady-state operating point of the circuit, and the response is similar to that of described in Section II-B for an output fault. However, in this case, the response of one LC circuit is affected by the load capacitance.

2) Resistive Load: In the case where a short-circuit fault occurs and $C_L = 0$ μF, the initial fault current is the sum of $i_{f,ZCB}$ and $i_{f,S}$. In this case, the voltage at both the input and the output collapses immediately. The initial fault current supplied by the dc source ($i_{f,S}$) is limited to I_L by the line inductance L_L. This means that the Z-source capacitance provides current to both the fault and load, i.e., it sees the fault in parallel with the load resistance. Thus, when the fault is a short circuit, the load resistance could be neglected. The thyristor current is forced to zero by $i_{f,ZCB}$ turning it OFF. After T_1 has turned OFF, L_1 current is clamped by D_5, and a series LC resonant circuit is formed through C_2, L_2, and the fault. The initial conditions for resonance are determined by the steady-state operating point of the circuit, and the response is similar to that of described in

Section II-B for an output fault. However, in this case, there is only one LC resonant circuit.

F. Minimum Detectable Fault Conductance—Input

In this section, the minimum detectable input fault conductance, $G_{f,min,in}$, is derived for the cases both with and without load capacitance.

1) RC Load: For the case where there is a load capacitance, when the input fault with conductance G_f occurs, the CB responds as described in Section II-E. The Z-source capacitors provide an initial fault voltage of V_S. Therefore, through analysis of the input node, the initial fault current is found to be

$$i_f(0) = i_{f,ZCB}(0) + i_{f,C}(0) + i_{f,S}(0). \tag{19}$$

The initial fault current is defined in terms of the fault conductance and the fault voltage as

$$i_f(0) = V_S G_f. \tag{20}$$

Because the initial current in inductors, L_1, L_2, and L_S, is equal to the steady-state load current, it is known that

$$i_{f,C}(0) = i_{f,S}(0) = I_L = \frac{V_S}{R_L}. \tag{21}$$

Thus, through substituting for $i_f(0)$ from (20) and for $i_{f,S}(0)$ and $i_{f,C}(0)$ from (21) into (19), it is found that

$$i_{f,ZCB}(0) = V_S G_f - 2\frac{V_S}{R_L}. \tag{22}$$

The minimum current $i_{f,ZCB}(0)$ that the CB requires to switch OFF is equal to the steady-state load current I_L. Therefore

$$G_{f,min,in} = \frac{3}{R_L}. \tag{23}$$

2) Resistive Load: For the case where there is no load capacitance, when an input fault of conductance G_f occurs, the CB responds as described in Section II-E. However, in this case, load resistance cannot be neglected, and the load is supplied with current $i_L(0)$. The Z-source capacitors provide an initial fault voltage of V_S. Therefore, through analysis of the input node, we have

$$i_f(0) = i_{f,ZCB}(0) + i_{f,S}(0) - i_L(0). \tag{24}$$

Because the initial voltages across capacitors C_1 and C_2 are equal to their steady-state voltages, it is known that

$$i_L(0) = \frac{v_{C_1}(0) + v_{C_2}(0)}{R_L} = \frac{V_S}{R_L}. \tag{25}$$

Thus, through substituting for $i_f(0)$, $i_{f,S}(0)$, and $i_L(0)$ from (20), (21), and, (25) respectively, into (24), we obtain

$$i_{f,ZCB}(0) = V_S \cdot G_f + \frac{V_S}{R_L} - \frac{V_S}{R_L}. \tag{26}$$

The minimum current $i_{f,ZCB}(0)$ that the CB requires to switch OFF is equal to the steady-state load current I_L. Therefore

$$G_{f,min,in} = \frac{1}{R_L}. \tag{27}$$

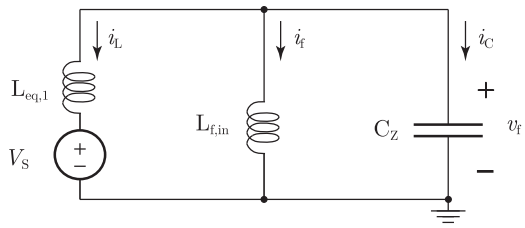

Fig. 4. Circuit model used to analyze $K_{rr,min,in}$.

The minimum input fault conductance required to trip the CB is larger for the case where there is load capacitance when compared with the case where there is no load capacitance. In the case where there is no load capacitance, $G_{f,min,in} = G_{f,min,out}$.

G. Minimum Detectable Frr–Input

In this section, the minimum detectable input Frr, $K_{rr,min,in}$, is derived. In this case, the fault conductance G_f is dependent on time t, as described in (10). To perform the numerical analysis, the fault impedance is taken to be an inductance (L_f), where

$$L_{f,in} \approx \frac{1}{K_{rr,in}}. \tag{28}$$

This approximation is described further in Section II-D. In a given system, the ZCB only trips autonomously for values of L_f lower than $L_{f,min,in}$. To find $K_{rr,min,in}$, the current through thyristor T_1 during the fault is analyzed. The circuit configuration used for analysis is the same as that shown in Fig. 3(b). In this case, it is assumed that C_L is large enough so that the output voltage is assumed to be constant during the turn-OFF period. This represents the worst scenario for $K_{rr,min,in}$. The analysis of current through T_1 can be broken into two time periods after the fault occurs at $t = 0$ μs. The first period is between $t = 0$ μs and $t = t_1$. During this period, D_2 and D_3 are switched ON, and the fault voltage is maintained at V_S as the source and CB current are commutated to the fault. Because the fault voltage is constant, the fault current increases according to

$$i_f(t) = \frac{V_S}{L_{f,in}} t, \quad \text{for } 0 < t < t_1. \tag{29}$$

The thyristor current is maintained;, thus

$$i_T(t) = \frac{V_S}{R_L}, \quad \text{for } 0 < t < t_1. \tag{30}$$

It is assumed that the change of $i_{f,S}$ and $i_{f,C}$ is small over the time period $0 \le t \le t_1$; thus

$$i_f(t_1) = 2I_L. \tag{31}$$

Through equating (29) and (31), and substituting for I_L from (21), it is found that

$$t_1 = \frac{2L_{f,in}}{R_L}. \tag{32}$$

At $t = t_1$, D_1 and D_4 are turned OFF. The second period is defined as $t_1 \le t \le t_2$. During this period, the circuit is modeled as shown in Fig. 4, where

$$L_{ZCB} = L_1 = L_2 \tag{33}$$

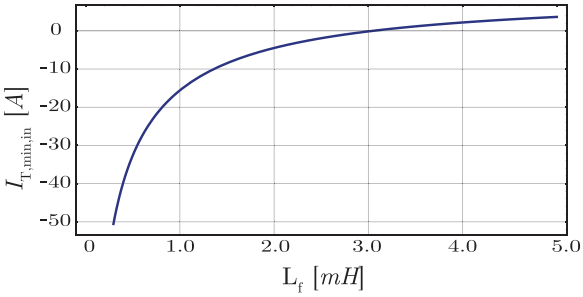

Fig. 5. Finding $L_{f,max,in}$ numerically as the inductance for which $I_{T,min,in} = 0$ A.

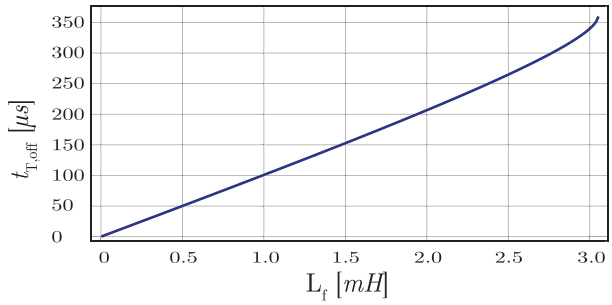

Fig. 6. Time taken for the thyristor current to fall to zero, $t_{T,off}$, versus fault inductance L_f.

$$C_Z = \left(\frac{1}{C_1} + \frac{1}{C_2}\right)^{-1} \tag{34}$$

$$L_{eq,1} = \left(\frac{1}{L_{f,in}} + \frac{1}{L_1 + L_2}\right)^{-1} \tag{35}$$

$$L_{eq,2} = \left(\frac{1}{L_{f,in}} + \frac{1}{2L_{ZCB}} + \frac{1}{L_f}\right)^{-1}. \tag{36}$$

The differential equation

$$\frac{d^2 v_f(t)}{dt^2} + \frac{1}{L_{eq,2}C_Z} v_f(t) = \frac{V_S}{L_{eq,1}C_Z}, \quad \text{for } t_1 < t \le t_2 \tag{37}$$

describes the fault voltage during this period. Solving this with initial conditions

$$v_f(t_1) = V_S \text{ and } \frac{dv_f}{dt}(t_1) = 0 \tag{38}$$

results in

$$v_f(t) = V_S \frac{L_{eq,2} + (L_{eq,1} - L_{eq,2})\cos(\frac{t}{\sqrt{L_{eq,2}C_Z}})}{L_{eq,1}}. \tag{39}$$

Note that, to solve (37), $t_1 = 0$ is assumed to simplify analysis. Once $v_f(t)$ is found, the thyristor current is derived to be

$$i_T(t) = \frac{V_S}{R_L} - V_S\sqrt{C_Z}\frac{(L_{eq,1} - L_{eq,2})\cos(\frac{t}{\sqrt{L_{eq,2}C_Z}})}{L_{eq,1}\sqrt{L_{eq,2}}} - V_S\frac{(L_{eq,1} - L_{eq,2})(\sqrt{C_Z L_{eq,2}}\sin(\frac{t}{\sqrt{L_{eq,2}C_Z}}) - t)}{L_{eq,1}(L_1 + L_2)}. \tag{40}$$

Then, $t_{min,in}$ at which i_T is minimum is found to be

$$t_{min,in} = \sqrt{L_{eq,2}C_Z}\cos^{-1}\left(\frac{L_{eq,2}}{L_{eq,1} + (L_1 + L_2)}\right). \tag{41}$$

Through substituting for C_Z, $L_{eq,1}$, $L_{eq,2}$, and $t_{min,in}$ from (34), (35), (36), and (41), respectively, in (40), $i_{T,min,in}$ is found as a function of L_f. Fig. 5 shows $i_{T,min,in}(L_f)$ for the parameters in Table III. The value of L_f, where $i_{T,min,in} = 0$ A, is $L_{f,max,in}$ for which the CB turns OFF. This is found numerically to be $L_{f,max,in} = 3.05$ mH. Thus, taking into account the initial assumption of (28), $K_{rr,min,in} = 327.87\ (\Omega \cdot s)^{-1}$.

The time taken for the thyristor current to fall to zero, ($t_{T,off}$), is also plotted for various values of L_f in Fig. 6. For values of L_f less than $L_{f,max,in}$, the relationship between L_f and $t_{T,off}$ is approximately linear with a gradient of 106 $\mu s \cdot mH^{-1}$.

TABLE I
PEAK CURRENT AND VOLTAGE IN COMPONENTS

Component	Peak Current	Peak Voltage	Comment
C_1 and C_2	i_{peak}	V_S	Z-source capacitors
L_1 and L_2	i_{peak}	V_S	Z-source inductors
T_1	I_L	V_S	Thyristor
D_1 and D_3	i_{peak}	V_S	Input diodes
D_2 and D_4	$2\ i_{peak}$	V_S	Output diodes

H. Component Maximum Currents and Voltages

The peak current and voltage stress on components occurs when the CB is operating at maximum load, and a short-circuit fault occurs. The peak current and voltage stress are required for selection of components.

The peak inductor, diode, and capacitor currents occur during the postfault resonance. The peak inductor current for the unidirectional series ZCB is derived in [27] as follows:

$$i_{peak} = I_L\sqrt{1 + 4Q^2} \tag{42}$$

where

$$Q = \frac{R_L}{2}\sqrt{\frac{C}{L}}. \tag{43}$$

These expression are used to find the peak currents in the proposed topology. Table I shows the peak currents and voltages across components during a short-circuit fault. This table assumes $R_1 = R_2 = 0$ and ideal semiconductors.

III. EVALUATION OF COMPETING PROPOSALS

This section provides an evaluation of existing ZCB topologies and comparison with the proposed topology. In this section, three existing bidirectional ZCBs, which are shown in Figs. 7–9, are described.

A. Bidirectional Topologies

Several ZCBs that allow bidirectional power flow have been proposed [30]–[32]. However, these have some disadvantages when compared with the proposed ZCB.

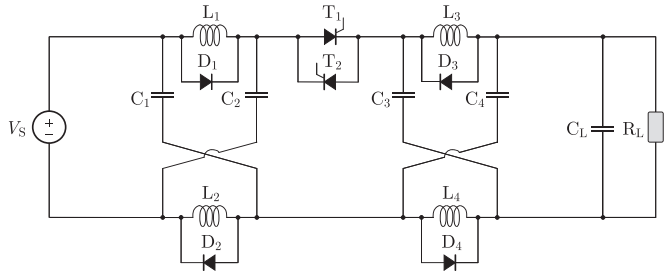

Fig. 7. Bidirectional ZCB topology presented in [24].

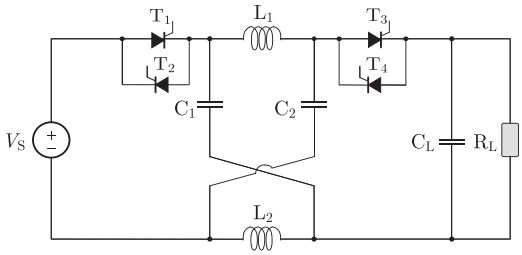

Fig. 8. Bidirectional ZCB topology presented in [24].

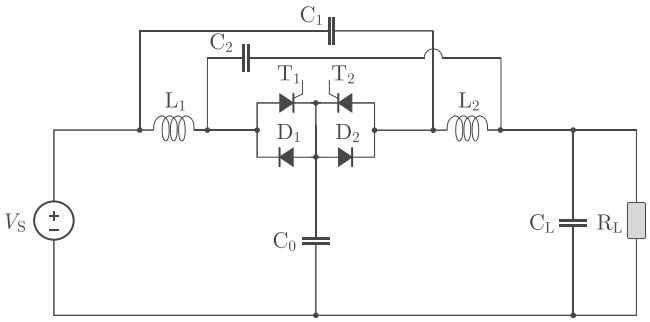

Fig. 9. Bidirectional ZCB topology presented in [30].

In [31], two bidirectional ZCBs are introduced. These are shown in Figs. 7 and 8. Both of these topologies are modifications of the classical ZCB [25]. As such, they do not have a common neutral or low-pass frequency response characteristic. A third bidirectional ZCB is introduced in [30] and is shown in Fig. 9. Its design has a combination of the characteristics of the series [26] and the parallel [24] ZCB topologies.

B. Topology Comparison

The comparison of the proposed bidirectional series ZCB with existing bidirectional ZCBs is given in Table II. It is seen that the proposed ZCB has a low number of passive components compared with other bidirectional ZCBs, which reduces size. Additionally, it has the fewest controlled switches, reducing unit cost, and complexity. The proposed ZCB is the only bidirectional ZCB that has a low-pass filter voltage transfer function, which allows it to be used for input filtering of power converters. Furthermore, the peak forward-blocking thyristor voltage is clamped in the proposed topology, which reduces component stress and cost compared with other topologies. Also, the proposed ZCB has a common neutral, which is required for earthed systems to limit current flowing through alternate return paths. Other topologies, without a common neutral, are unsuitable for earthed systems.

In ZCBs, a current spike occurs in the thyristor when it commutates OFF. This is due to its reverse recovery characteristic. If the current spike is propagated to the input of the ZCB, it may cause issues with CB coordination. The proposed ZCB does not propagate this spike to its input, while the other bidirectional topologies do.

The reverse voltage applied to the thyristor assists causes it to commutate OFF. With low reverse voltages, the turn-off time of the thyristor is increased [33]. The reverse voltage is not limited in the proposed CB and is approximately equal to the source voltage. However, for the topology in Fig. 9, antiparallel diodes across each thyristor limit the reverse voltage of the thyristor during commutation, which increases its turn-off time (t_q).

One disadvantage of the proposed topology is that it reflects a portion of the fault current to the source when interrupting a fault at its output. However, in [29], it is shown that the reflected fault current can be reduced to zero by replacing the inductors with mutually coupled ones, though this, in turn, requires a lower thyristor turn-off time.

IV. Performance Evaluation

This section presents simulation and experimental results that validate the aforementioned operation of the proposed ZCB topology. Section IV-A presents detailed simulation results and discussion of the proposed ZCB topology over a range of different fault conditions. Additionally, in Section IV-B, using an experimental setup, the performance of the proposed ZCB is experimentally validated.

A. Simulation Results

To evaluate the performance of the proposed CB, a test system, as shown in Fig. 2, is simulated in the MATLAB/Simulink environment. The parameters of the simulated system are set according to Table III, except where explicitly stated otherwise. The simulated system is used to evaluate the performance of the proposed ZCB and to verify the expressions presented in Section II. In all simulation tests, the CB is in the steady state before the fault is applied.

1) Infinite Fault Conductance: First, a bolted fault is applied to the CB's output at $t = 0$ μs, for the case where $L_L = 0$ mH. This provides a base case of the CB's operation. The CB's response to the fault is shown in Fig. 10. This response is consistent with the description given in Section II-B. After the fault occurs, i_T, as shown in Fig. 10(b), falls to zero immediately due the fault current supplied by the Z-source capacitance, $i_{f,ZCB}$. The LC resonant response of the inductors and capacitors occurs between $0 < t < 260$ μs. At $t = 260$ μs, the inductor currents are clamped by D_5 and D_6. Thus, the inductor currents, shown in Fig. 10(a), decay rapidly through the clamping diodes and resistors. When the inductors are clamped, the input and output currents, shown in Fig. 10(c), rapidly fall to zero.

It is also observed that the peak output current is twice the peak input current. Thus, the peak current in D_4 is twice that of D_1. After the thyristor is disconnected, both LC resonant circuits

TABLE II
BIDIRECTIONAL ZCB COMPARISON

Category		Fig. 7 [31]	Fig. 8 [31]	Fig. 9 [30]	Proposed Fig. 2
1	Number of Passive Components	8	4	5	4
2	Number of Controlled Switches	2	4	2	1
3	Common Neutral	No	No	Yes	Yes
4	Suitable for Input Filtering of Power Converters	No	No	No	Yes
5	Peak Forward-Blocking Voltage of Thyristor	V_S	$> V_S$	$> V_S$	V_S
6	Input Current Spike due to Reverse Recovery of Thyristor	Yes	Yes	Yes	No
7	Limited Peak Thyristor Reverse Resonance Voltage	No	No	Yes	No
8	Magnitude of Reflected Fault Current	Zero	Zero	High	Moderate

TABLE III
EXPERIMENTAL SETUP COMPONENT VALUES

Parameter	Value	Comment
$C_1 = C_2 = C$	33 μF	Z-source capacitors
$L_1 = L_2 = L$	1 mH	Z-source inductors
R_L	30 Ω	Load resistance
V_S	300 V	Source voltage
R_C	1 Ω	Clamping resistor
L_L	5 mH	Line inductance
C_L	480 μF	Load capacitance

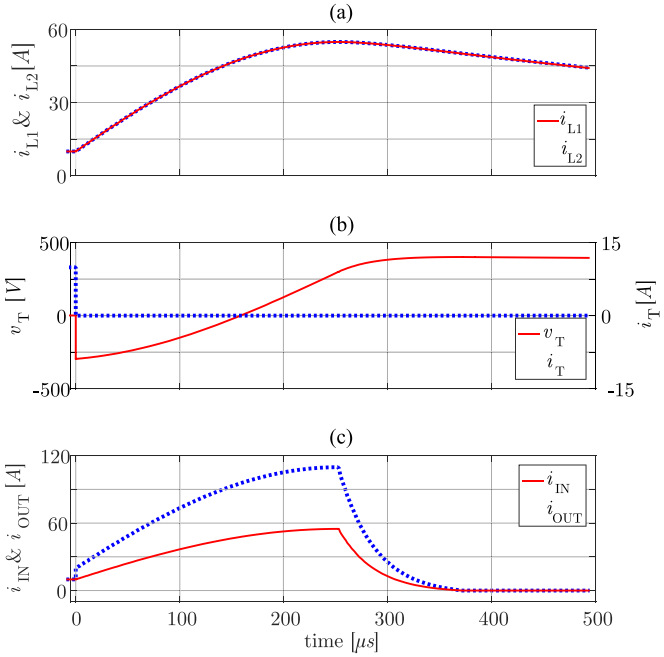

Fig. 10. Simulation results for a bolted fault on CB output. (a) Inductor currents. (b) Thyristor voltage and current. (c) Input and output currents.

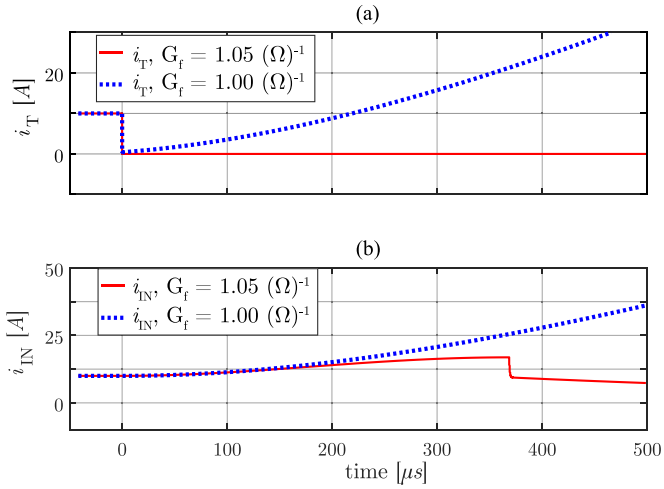

Fig. 11. Simulation results for output faults $G_f = 1.05$ $(\Omega)^{-1}$ and $G_f = 1.00$ $(\Omega)^{-1}$, where $C_L = 500$ μF. (a) Thyristor currents and (b) input currents.

are connected in series with the output. Thus, the output current is the summation of their individual currents. Conversely, only the LC circuit containing L_1 and C_1 is connected in series with the input.

The reverse resonance time (t_{rr}) is the time for which the thyristor remains reverse biased during turn OFF. In this simulation, it is measured as $t_{rr,out,sim} = 158.9$ μs. In order for the thyristor to remain OFF, t_{rr} must be greater than the thyristor's turn-off time (t_q). A line inductance $L_L = 1$ mH is added to the model, and the simulation is repeated with the fault induced on the CB's input terminals. In this case, $t_{rr,in,sim} = 159.3$ μs. The two measured values are close to the value calculated, $t_{rr,calc} = 159.0$ μs, using the expression derived in [27] for the series ZCB.

2) Minimum Fault Conductance:

a) Output: This simulation test is performed to validate the expression for minimum output fault conductance as expressed in (9). The calculated minimum fault conductance for the component values in Table III is $G_{f,min,out} = 1.043$ $(\Omega)^{-1}$. Therefore, simulation tests are carried out for values slightly above and below the minimum fault conductance, $G_f = 1.05$ $(\Omega)^{-1}$ and $G_f = 1.00$ $(\Omega)^{-1}$, respectively. The thyristor and input currents are shown in Fig. 11.

As shown in Fig. 11(a), for $G_f = 1.05$ $(\Omega)^{-1}$, before the fault, i_T is at a steady-state value of 10 A. When the fault occurs at $t = 0$ μs, i_T is rapidly forced to zero. Thus, the CB switches OFF. As shown in Fig. 11(b), i_{IN} is also at a steady-state value of 10 A before the fault. When the fault occurs, i_{IN} begins to rise and reaches a peak value of 16.9 A. This peak input current is lower than the case where there is no fault impedance, due to damping of the resonant response of the series LC circuits. Additional damping is created by the series fault resistance.

For the case where $G_f = 1.00$ $(\Omega)^{-1}$, i_T is shown in Fig. 11(a). Prior to the fault, i_T is at a steady-state value of 10 A. When the

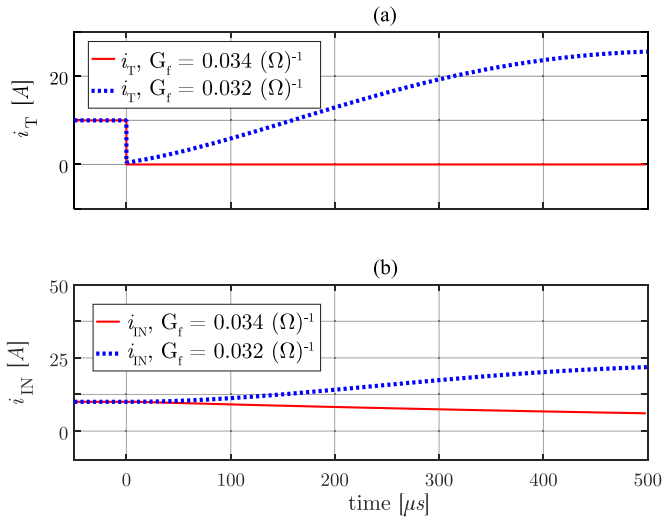

Fig. 12. Simulation results for output faults $G_f = 0.034$ $(\Omega)^{-1}$ and $G_f = 0.032$ $(\Omega)^{-1}$, where $C_L = 0$ μF. (a) Thyristor currents and (b) input currents.

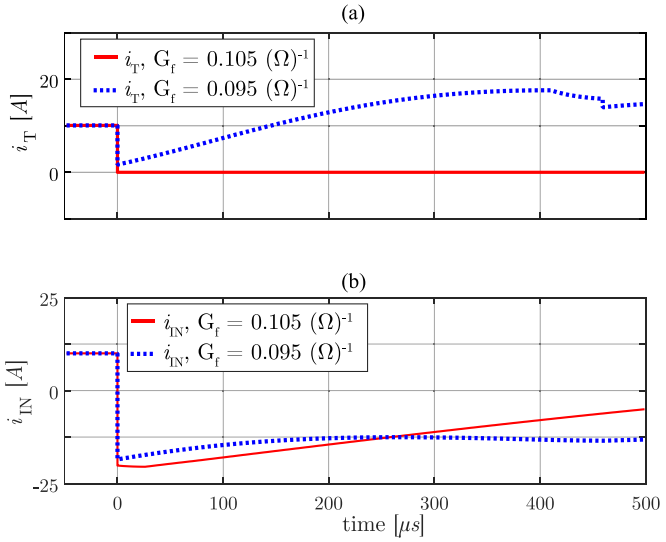

Fig. 13. Simulation results for input faults $G_f = 0.105$ $(\Omega)^{-1}$ and $G_f = 0.095$ $(\Omega)^{-1}$, where $C_L = 500$ μF. (a) Thyristor currents and (b) input currents.

fault occurs at $t = 0$ μs, the fault current flowing through the Z-source capacitors is not enough to overcome the steady-state load current and to force i_T to zero. Thus, the CB does not trip, and the fault current continues to increase through the thyristor. As shown in Fig. 11(b), i_{IN} is also at a steady-state value of 10 A before the fault. When the fault occurs at $t = 0$ μs, because the CB does not turn OFF, i_{IN} rises. This response is dominated by the characteristics of the Z-source inductance.

The simulation test is then repeated with $C_L = 0$ μF. The minimum fault conductance calculated using (9) in this case is $G_{f,min,out} = 0.033$ $(\Omega)^{-1}$. Two simulation tests are carried out for $G_f = 0.034$ $(\Omega)^{-1}$ and $G_f = 0.032$ $(\Omega)^{-1}$. The thyristor and input currents are shown in Fig. 12.

For the case where $G_f = 0.034$ $(\Omega)^{-1}$, i_T is shown in Fig. 12(a). Prior to the fault, i_T is at a steady-state value of 10 A. When the fault occurs at $t = 0$ μs, i_T falls rapidly to zero. Thus, the CB switches OFF. As shown in Fig. 12(b), i_{IN} is also at a steady-state value of 10 A before the fault. When the fault occurs, i_{IN} begins to fall immediately. In this case, there is no resonant response of i_{IN}. The reason is that the large fault resistance overdamps the series LC circuits created when the CB opens.

For the case where $G_f = 0.032$ $(\Omega)^{-1}$, i_T is shown in Fig. 12(a). Prior to the fault, i_T is at a steady-state value of 10 A. The fault occurs at $t = 0$ μs; however, current flowing through the Z-source capacitors is not enough to overcome the steady-state load current. Thus, the CB does not trip. As shown in Fig. 12(b), i_{IN} is also at a steady-state value of 10 A before the fault. When the fault occurs at $t = 0$ μs, because the CB does not turn OFF, i_{IN} rises. This response is dominated by the characteristics of the Z-source inductance.

The case where there is no load capacitance defines a fundamental limit on minimum output fault conductance, which is equal to the load conductance. The CB cannot be designed to trip autonomously for the fault conductance less than the load conductance.

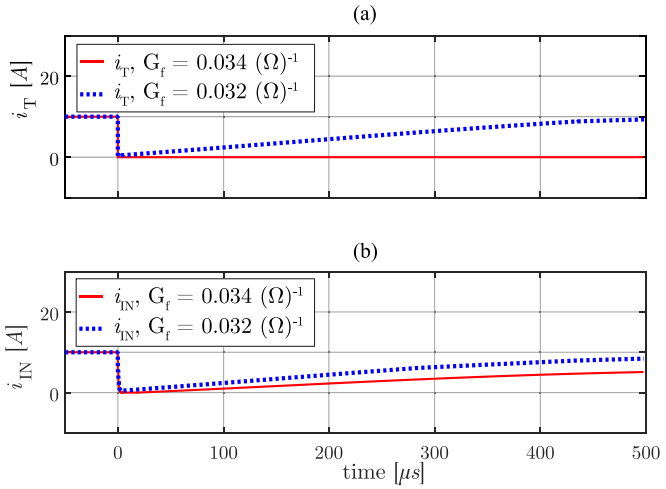

Fig. 14. Simulation results for input faults $G_f = 0.034$ $(\Omega)^{-1}$ and $G_f = 0.032$ $(\Omega)^{-1}$, where $C_L = 0$ μF. (a) Thyristor currents and (b) input currents.

b) Input: A simulation test is carried out for faults on the CB's input. The minimum fault conductances for cases both with and without a load capacitance are calculated according to (23) and (27). With a load capacitance $C_L = 500$ μF, $G_{f,min,in} = 0.1$ $(\Omega)^{-1}$, and with a load capacitance $C_L = 0$ μF, $G_{f,min,in} = 0.033$ $(\Omega)^{-1}$. The simulation tests are carried out for both $G_f = 0.105$ $(\Omega)^{-1}$ and $G_f = 0.095$ $(\Omega)^{-1}$ with $C_L = 500$ μF. The results are shown in Fig. 13. It is noted that when $G_f = 0.105$ $(\Omega \cdot s)^{-1}$, the thyristor switches OFF. However, the input current continues to rise. Although this is true for the time period shown, the current decays after $t = 500$ μs. For the case where $G_f = 0.095$ $(\Omega)^{-1}$, the thyristor current does not drop below zero; thus, the CB does not trip.

Additionally, simulation tests are carried out for $G_f = 0.032$ $(\Omega)^{-1}$ and $G_f = 0.034$ $(\Omega)^{-1}$, with $C_L = 0$ μF. The results are shown in Fig. 14. As expected, a fault conductance

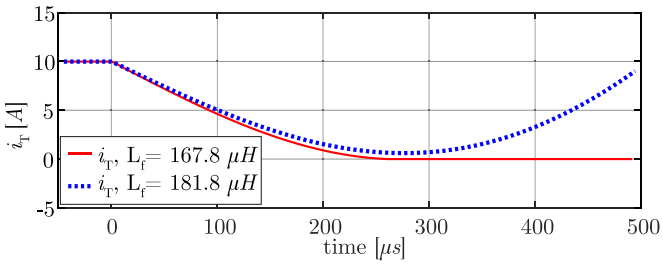

Fig. 15. Simulation of thyristor current during output faults with inductances $L_f = 167.8\ \mu H$ and $L_f = 181.8\ \mu H$, where $C_L = 500\ \mu F$.

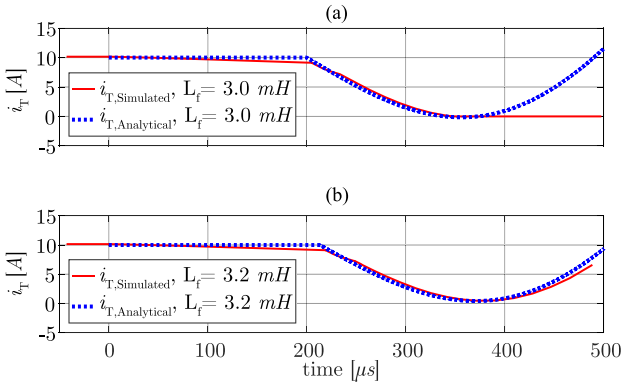

Fig. 16. Simulation results for input fault, $L_f = 3$ mH and $L_f = 3.2$ mH, where $C_L = 500\ \mu F$, compared with analytically modeled equations (40) and (41).

of $G_f = 0.034\ (\Omega)^{-1}$ switches the thyristor OFF, while a fault conductance of $G_f = 0.032\ (\Omega)^{-1}$ does not.

3) Minimum Frr:

a) Output: The minimum output Frr, which causes the CB to switch OFF, is also investigated through simulation. To do this, an inductance L_f is placed in series with the fault. This approximates the characteristics of a conductance with ramp K_{rr}, as described in Section II-D. The minimum Frr that trips the CB is calculated using (17) to be $K_{rr,min,in} = 5730\ (\Omega \cdot s)^{-1}$. In Fig. 15, the simulated thyristor current is shown for the cases where faults with inductances of $L_f = 167.8\ \mu H$ and $L_f = 181.8\ \mu H$ are applied to the CB's output. These values correspond to fault conductance ramp rates of $K_{rr} = 5500\ (\Omega \cdot s)^{-1}$ and $K_{rr} = 5960\ (\Omega \cdot s)^{-1}$, respectively. For the case where $L_f = 167.8\ \mu H$, i_T falls gradually to zero, and the thyristor switches OFF. However, for the case where $L_f = 181.8\ \mu H$, the thyristor current does not fall to zero; thus, the thyristor remains in the conducting state, and the CB does not trip.

b) Input: A simulation is used to evaluate the analytical modeling in Section II-G. In Section II-G, a method is presented for finding $L_{f,max,in}$. For the component values in Table III, $L_{f,max,in} = 3.05$ mH. Therefore, the CB system is simulated to find the thyristor current ($i_{T,Simulated}$) with input faults of inductances $L_f = 3$ mH and $L_f = 3.2$ mH. These correspond to inductances below and above the maximum input fault inductance. The analytical thyristor current ($i_{T,Analytical}$) is also found using (40) for the two inductance values. This allows a comparison of the $i_{T,Analytical}$ with $i_{T,Simulated}$ to be made in Fig. 16.

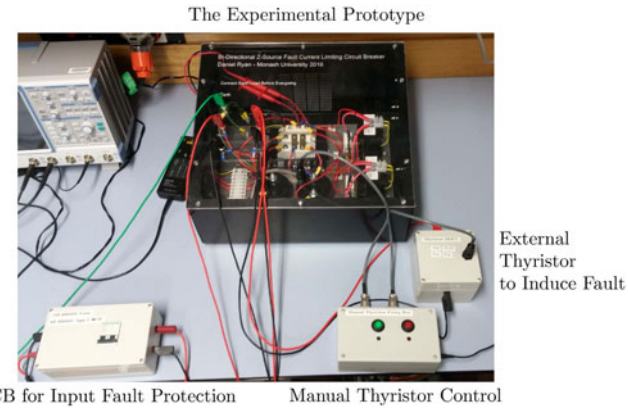

Fig. 17. Experimental prototype.

In Fig. 16(a), $i_{T,Simulated}$ and $i_{T,Analytical}$ are shown for the case where $L_f = 3$ mH. It is seen that the simulated and analytical results match closely. Fig. 16(a) also shows that the CB trips (i.e., $i_{T,Simulated}$ and $i_{T,Analytical}$ fall to/below 0 A), which is expected for the fault inductance below $L_{f,max,in}$. It is noted that $i_{T,Analytical}$ rises again after falling to zero. This is because the nonlinear switching of the thyristor is not part of the analytical model. In Fig. 16(b), $i_{T,Simulated}$ and $i_{T,Analytical}$ are shown for the case where $L_f = 3.2$ mH; it is seen that the simulated and analytical results match closely. Fig. 16(b) also shows that the CB does not trip (i.e., $i_{T,Simulated}$ and $i_{T,Analytical}$ do not fall to/below 0 A), which is expected for the fault inductance above $L_{f,max,in}$. These results confirm the analytical model and the method for finding $L_{f,max,in}$ presented in Section II-G.

B. Experimental Results

To experimentally validate the findings, an experimental prototype is implemented with the selected component values shown in Table III. A photo of the implemented ZCB is shown in Fig. 17.

1) Output Fault: To demonstrate the prototype's bidirectional capability, it is tested in both the forward and reverse directions. Initially, one pair of input terminals is connected to a dc voltage source, and the other is connected to a resistive load. In the first test, the initial steady-state operating current is 10 A. At $t = 50\ \mu s$, a fault is applied across the load. The inductor currents, thyristor voltage, thyristor current, input current, and output current are shown in Fig. 18. In Fig. 18(a), it is seen that both inductor currents increase gradually when the fault occurs and then begin to decay as they are clamped by their reverse-biased clamping diodes. The thyristor current and voltage in Fig. 18(b) show that immediately after the fault, the thyristor switches OFF and remains reverse biased for t_{rr}. However, a negative voltage spike is observed in the thyristor current that is not observed in simulation. This is due to the thyristor reverse recovery characteristic. The peak of this spike is dependent on the reverse recovery charge of the thyristor and rate of current fall [33]. Although this spike is propagated through the CB capacitors, the thyristor, and the output diode, it is not experienced on the input. Thus, the reverse recovery current spike of the main

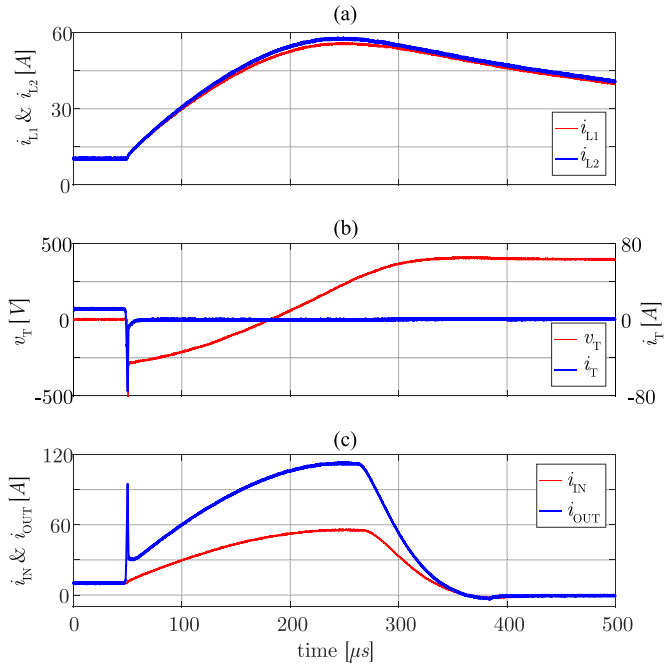

Fig. 18. Experimental results for a direct fault on the output with the ZCB in the forward direction. (a) Inductor currents. (b) Thyristor voltage and current. (c) Input and output current.

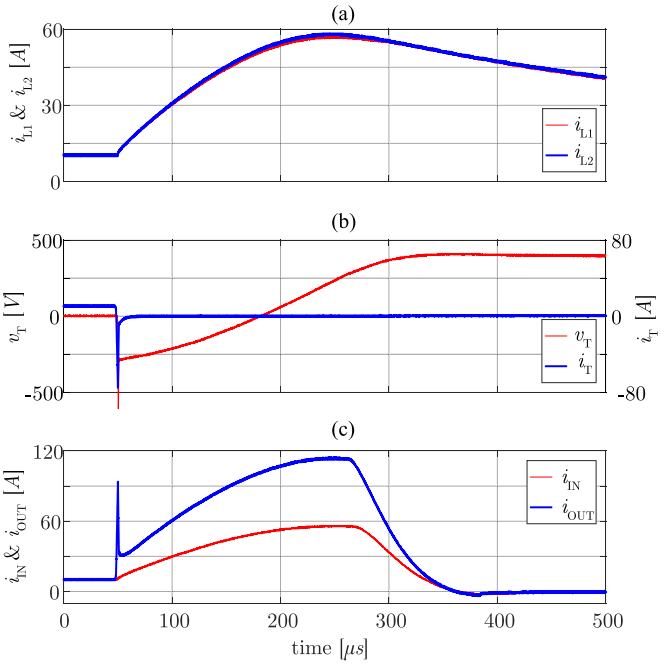

Fig. 19. Experimental results for a direct fault on the output with the ZCB in the reverse direction. (a) Inductor currents. (b) Thyristor voltage and current. (c) Input and output current.

thyristor switch does not have any impact on coordination with upstream CBs. In Fig. 18(c), the CB input and output currents are shown. It is seen that the reverse recovery current spike is propagated to the CBs output, though it is lower in magnitude than the maximum output current.

The experiment described above is then repeated after switching the source and load terminals of the CB. The inductor currents are shown in Fig. 19(a), thyristor voltage and thyristor current are shown in Fig. 19(b), and input current and output current are shown in Fig. 19(c). It is observed that these results closely match those with the CB the forward direction, confirming that the CB's response is not dependent on its orientation.

The reverse resonance time t_{rr} for forward- and reverse-oriented cases described above is measured to be 132.6 and 132.0 μs, respectively, which is lower than the time expected from simulation. This can be explained by the derating of inductors L_1 and L_2 due to the large dc bias current. Therefore, the inductance values are derated by 30%. The reverse resonance time with this lower inductance is calculated to be 137.0 μs using the expression derived in [27], which is in agreement with the experimental results. This effect is observed due to core nonlinearity, which causes inductance to decrease at high dc bias currents. A dc bias derating is also observed in an experimental prototype of the unidirectional series ZCB in [27].

2) Resistive Output Fault: To verify (9), a 480–μF capacitance is added in parallel with the resistive load. Thus, according to (9), $G_{f,min,out} = 1.003\ (\Omega)^{-1}$. Therefore, faults with conductances of $1.136\ (\Omega)^{-1}$ and $0.833\ (\Omega)^{-1}$, respectively, are applied to the CBs output. Initially, the steady-state operating current is 10 A. At $t = 50\ \mu$s, the fault is applied across the load. The

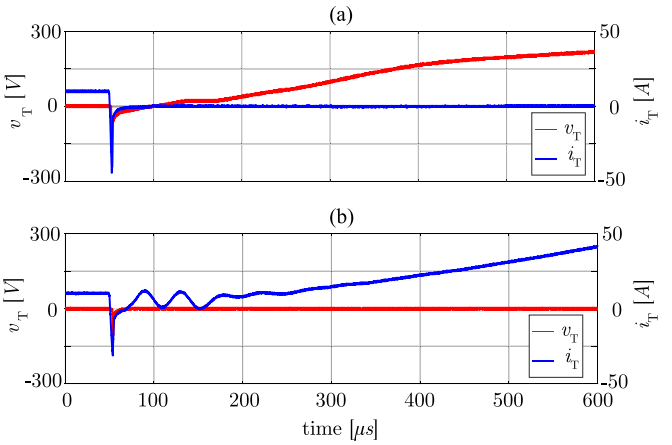

Fig. 20. Experimental results for a resistive fault on the output of the ZCB. (a) Thyristor voltage and current, where $G_{f,out} = 1.136\ (\Omega)^{-1}$. (b) Thyristor voltage and current, where $G_{f,out} = 0.833\ (\Omega)^{-1}$.

thyristor current and voltage during these tests are shown in Fig. 20.

These results verify expression (9). It is seen that for $G_f > G_{f,min,out}$, the thyristor current falls to zero, and its forward voltage increases (forward blocking). Thus, the CB is tripped. For $G_f < G_{f,min,out}$, the thyristor current continues to rise, and its forward voltage stays low (forward conducting). Thus, the CB is not tripped.

One discrepancy between the experimental results in Fig. 20 and simulation results shown in Fig. 11 is noted. For the case where $G_f < G_{f,min,out}$, the thyristor current did fall briefly to zero. Additionally, there is significant ringing in the thyristor current. This occurs due to parasitic inductance between the CB and the load capacitor. As the parasitic inductance decreases

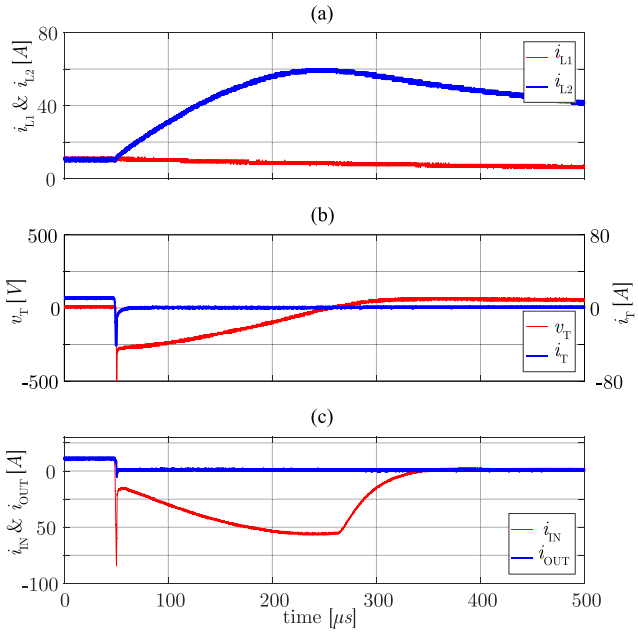

Fig. 21. Experimental results for a direct fault on the input of the ZCB. (a) Inductor currents. (b) Thyristor voltage and current. (c) Input and output current.

the minimum fault conductance, (9) is conservative when the parasitic inductance is taken into account.

3) Input Fault: For this test, the system is reconfigured through adding an additional 5-mH inductance between the voltage source and CB. The initial operating voltage is 300 V. At $t = 50$ μs, a fault is applied across the input of the CB. The inductor currents are shown in Fig. 21(a). The thyristor voltage and current are shown in Fig. 21(b), and the input and output currents are shown in Fig. 21(c). It is observed that when the fault occurs, the thyristor current undergoes a reverse recovery transient and then falls to zero. Thus, the CB turns OFF. However, the reverse resonance time of the thyristor voltage is increased when compared with the case of an output fault described in Section IV-B1. This is due to the circuit configuration immediately after the thyristor switches OFF. It is observed the current in inductor L_1 begins to decay immediately after the fault. This is because it is clamped by its freewheeling diode as the input voltage collapses. This clamps the thyristors anode to 0 V. Thus, the response of v_T is only due to the resonant response of L_2 and C_2. The output current of the CB falls immediately to zero when the fault occurs, and the input current waveform looks similar to that for an output fault. However, in this case, the current has an opposite sign. This is because current flows from energy stored in the CB to the fault.

V. Conclusion

In this paper, a bidirectional series ZCB is presented. It maintains the advantages of the unidirectional series ZCB over other ZCB topologies, yet it allows bidirectional current flow. It is first introduced. Then, the CB's response to faults is analyzed for a simple power system. This allows development of useful expressions for the minimum fault conductances and Frrs that trip the CB. These expressions are verified through computer simulation. Additionally, an experimental prototype is implemented and tested for several fault cases, which demonstrate the CB's bidirectional power flow capability and ability to break fault currents for faults on either the load or source side.

References

[1] B. Zahedi and L. E. Norum, "Modeling and simulation of all-electric ships with low-voltage DC hybrid power systems," *IEEE Trans. Power Electron.*, vol. 28, no. 10, pp. 4525–4537, Oct. 2013.

[2] N. Flourentzou, V. G. Agelidis, and G. D. Demetriades, "VSC-based HVDC power transmission systems: An overview," *IEEE Trans. Power Electron.*, vol. 24, no. 3, pp. 592–602, Mar. 2009.

[3] T. Dragievi, X. Lu, J. C. Vasquez, and J. M. Guerrero, "DC microgrids—Part I: A review of control strategies and stabilization techniques," *IEEE Trans. Power Electron.*, vol. 31, no. 7, pp. 4876–4891, Jul. 2016.

[4] F. Nejabatkhah and Y. W. Li, "Overview of power management strategies of hybrid AC/DC microgrid," *IEEE Trans. Power Electron.*, vol. 30, no. 12, pp. 7072–7089, Dec. 2015.

[5] E. Candan, P. S. Shenoy, and R. C. N. Pilawa-Podgurski, "A series-stacked power delivery architecture with isolated differential power conversion for data centers," *IEEE Trans. Power Electron.*, vol. 31, no. 5, pp. 3690–3703, May 2016.

[6] P. Rakhra, P. J. Norman, S. D. A. Fletcher, S. J. Galloway, and G. M. Burt, "Evaluation of the impact of high-bandwidth energy-storage systems on DC protection," *IEEE Trans. Power Del.*, vol. 31, no. 2, pp. 586–595, Apr. 2016.

[7] Q. Wei, B. Wu, D. Xu, and N. R. Zargari, "A medium-frequency transformer-based wind energy conversion system used for current-source converter-based offshore wind farm," *IEEE Trans. Power Electron.*, vol. 32, no. 1, pp. 248–259, Jan. 2017.

[8] R. M. Cuzner and G. Venkataramanan, "The status of DC micro-grid protection," in *Proc. IEEE Ind. Appl. Soc. Annu. Meeting*, 2008, pp. 1–8.

[9] M. Kempkes, I. Roth, and M. Gaudreau, "Solid-state circuit breakers for medium voltage DC power," in *Proc. IEEE Electr. Ship Technol. Symp.*, 2011, pp. 254–257.

[10] M. Heidemann, G. Nikolic, A. Schnettler, A. Qawasmi, N. Soltau, and R. W. D. Donker, "Circuit-breakers for medium-voltage DC grids," in *Proc. IEEE PES Transmiss. Distrib. Conf. Expo.-Latin Amer.*, 2016, pp. 1–6.

[11] A. Emhemed, K. Fong, S. Fletcher, and G. Burt, "Validation of fast and selective protection scheme for an LVDC distribution network," *IEEE Trans. Power Del.*, vol. 32, no. 3, pp. 1432–1440, Jun. 2017.

[12] C. Meyer, S. Schroder, and R. W. D. Doncker, "Solid-state circuit breakers and current limiters for medium-voltage systems having distributed power systems," *IEEE Trans. Power Electron.*, vol. 19, no. 5, pp. 1333–1340, Sep. 2004.

[13] F. Agostini *et al.*, "1MW bi-directional DC solid state circuit breaker based on air cooled reverse blocking-IGCT," in *Proc. IEEE Electr. Ship Technol. Symp.*, 2015, pp. 287–292.

[14] Y. Sato, Y. Tanaka, A. Fukui, M. Yamasaki, and H. Ohashi, "SiC-SIT circuit breakers with controllable interruption voltage for 400-V DC distribution systems," *IEEE Trans. Power Electron.*, vol. 29, no. 5, pp. 2597–2605, May 2014.

[15] Z. J. Shen, G. Sabui, Z. Miao, and Z. Shuai, "Wide-bandgap solid-state circuit breakers for DC power systems: Device and circuit considerations," *IEEE Trans. Electron Devices*, vol. 62, no. 2, pp. 294–300, Feb. 2015.

[16] R. M. Cuzner and V. Singh, "Future shipboard MVDC system protection requirements and solid-state protective device topological tradeoffs," *IEEE J. Emerg. Sel. Topics Power Electron.*, vol. 5, no. 1, pp. 244–259, Mar. 2017.

[17] L. L. Qi, A. Antoniazzi, L. Raciti, and D. Leoni, "Design of solid-state circuit breaker-based protection for DC shipboard power systems," *IEEE J. Emerg. Sel. Topics Power Electron.*, vol. 5, no. 1, pp. 260–268, Mar. 2017.

[18] H. Polman, J. A. Ferreira, M. Kaanders, B. H. Evenblij, and P. V. Gelder, "Design of a bi-directional 600 V/6 kA ZVS hybrid DC switch using IGBTS," in *Proc. Conf. Rec. 36th IAS Annu. Meeting IEEE Ind. Appl. Conf.*, 2001, vol. 2, pp. 1052–1059.

[19] J. M. Meyer and A. Rufer, "A DC hybrid circuit breaker with ultra-fast contact opening and integrated gate-commutated thyristors (IGCTS)," *IEEE Trans. Power Del.*, vol. 21, no. 2, pp. 646–651, Apr. 2006.

[20] A. Hassanpoor, J. Hfner, and B. Jacobson, "Technical assessment of load commutation switch in hybrid HVDC breaker," *IEEE Trans. Power Electron.*, vol. 30, no. 10, pp. 5393–5400, Oct. 2015.
[21] X. Song, C. Peng, and A. Huang, "A medium voltage hybrid DC circuit breaker; Part I: Solid state main breaker based on 15 kV SiC emitter turn-OFF (ETO) thyristor," *IEEE J. Emerg. Sel. Topics Power Electron.*, vol. 5, no. 1, pp. 278–288, Mar. 2017.
[22] D. Dring, D. Ergin, K. Wrflinger, J. Dorn, F. Schettler, and E. Spahic, "System integration aspects of dc circuit breakers," *IET Power Electron.*, vol. 9, no. 2, pp. 219–227, 2016.
[23] D. Bsche, E. D. Wilkening, H. Kpf, and M. Kurrat, "Hybrid dc circuit breaker feasibility study," *IEEE Trans. Compon., Packag., Manuf. Technol.*, vol. 7, no. 3, pp. 354–362, Mar. 2017.
[24] K. A. Corzine and R. W. Ashton, "A new Z-source DC circuit breaker," *IEEE Trans. Power Electron.*, vol. 27, no. 6, pp. 2796–2804, Jun. 2012.
[25] K. A. Corzine and R. W. Ashton, "A new Z-source DC circuit breaker," in *Proc. IEEE Int. Symp. Ind. Electron.*, 2010, pp. 585–590.
[26] A. H. Chang, A. T. Avestruz, S. B. Leeb, and J. L. Kirtley, "Design of DC system protection," in *Proc. IEEE Electr. Ship Technol. Symp.*, 2013, pp. 500–508.
[27] A. H. Chang, B. R. Sennett, A. T. Avestruz, S. B. Leeb, and J. L. Kirtley, "Analysis and design of DC system protection using z-source circuit breaker," *IEEE Trans. Power Electron.*, vol. 31, no. 2, pp. 1036–1049, Feb. 2016.
[28] A. Maqsood, A. Overstreet, and K. Corzine, "Modified Z-source DC circuit breaker topologies," *IEEE Trans. Power Electron.*, vol. 31, no. 10, pp. 7394–7403, Oct. 2016.
[29] A. Maqsood and K. Corzine, "Z-source DC circuit breakers with coupled inductors," in *Proc. IEEE Energy Convers. Congr. Expo.*, 2015, pp. 1905–1909.
[30] D. Keshavarzi, T. Ghanbari, and E. Farjah, "A Z-source based bidirectional DC circuit breaker with fault current limitation and interruption capabilities," *IEEE Trans. Power Electron.*, vol. 32, no. 9, pp. 6813–6822, Sep. 2017.
[31] A. Maqsood and K. Corzine, "The z-source breaker for fault protection in ship power systems," in *Proc. Int. Symp. Power Electron., Elect. Drives, Autom. Motion.*, 2014, pp. 307–312.
[32] A. Maqsood, L. Lu, and K. A. Corzine, "Low-voltage DC testbed design for a Z-source breaker based protection scheme," in *Proc. Clemson Univ. Power Syst. Conf.*, 2016, pp. 1–6.
[33] A. Wintrich, U. Nicolai, W. Tursky, and T. Reimann, *Application Manual Power Semiconductors*. 2nd ed. Nuremberg, Germany: Semikron Int., 2015.

Daniel Joseph Ryan (S'16) received the B.E. (Hons.) degree in electrical and computer systems engineering in 2015 from Monash University, Melbourne, VIC, Australia, where he is currently working toward the Ph.D. degree.

His research interests include protection of dc power systems, grid integration of energy storage, and power system dynamics and control.

Hugh Duffy Torresan (M'05) received the B.E. (Hons.) degree in electrical and computer systems engineering and the master's degree in engineering science (research) from Monash University, Melbourne, VIC, Australia, in 2002 and 2005, respectively. In 2008, he completed the Submarine Design and Procurement course with University College London, London, U.K., and qualified for Chartered Engineer status with the Royal Institution of Naval Architect (RINA) and the British Engineering Council in 2011.

He led Defence Science and Technology (DST) Group's, Melbourne, contribution to The Technical Co-operation Program (TCCP) on Power and Energy Materials and Systems from 2006 to 2015, culminating in five years as the Panel Chair. He is a Senior Electrical Research Engineer with the Maritime Division of DST Group and the Chair of the Victorian Section of RINA. He leads DST Group's science program on maritime batteries and provides research support to both the Royal Australian Navy's in-service fleet, as well as new-build projects. His research interests include deep learning for battery performance prediction, statistical models of large-format battery installations, and novel application of imbricated cell inverters.

Behrooz Bahrani (M'07) received the B.Sc. degree from Sharif University of Technology, Tehran, Iran, the M.Sc. degree from the University of Toronto, Toronto, ON, Canada, and the Ph.D. degree from the Ecole Polytechnique Fédérale de Lausanne (EPFL), Lausanne, Switzerland, in 2006, 2008, and 2012, respectively, all in electrical engineering.

From September 2012 to September 2015, he was a Postdoctoral Fellow at several institutions including EPFL, Purdue University, West Lafayette, IN, USA, Georgia Institute of Technology, Atlanta, GA, USA, and the Technical University of Munich, Munich, Germany. He is currently a Lecturer with Monash University, Melbourne, VIC, Australia. His research interests include control of power electronic systems, applications of power electronics in power and traction systems, and grid integration of renewable energy resources.